

# Generalized Diffusion Simulation-Based Tractography \*

Qi Zhuang <sup>†</sup>, Brian T. Gold <sup>‡</sup>, Ruiwang Huang <sup>§</sup>,  
Xuwei Liang <sup>¶</sup>, Ning Cao <sup>||</sup>, and Jun Zhang<sup>\*\*</sup>

## Abstract

Diffusion weighted imaging (DWI) techniques have been used to study human brain white matter fiber structures *in vivo*. Commonly used standard diffusion tensor magnetic resonance imaging (DTI) tractography derived from the second order diffusion tensor model has limitations in its ability to resolve complex fiber tracts. We propose a new fiber tracking method based on the generalized diffusion tensor (GDT) model. This new method better models the anisotropic diffusion process in human brain by using the generalized diffusion simulation-based fiber tractography (GDST). Due to the additional information provided by GDT, the GDST method simulates the underlying physical diffusion process of the human brain more accurately than does the standard DTI method. The effectiveness of the new fiber tracking algorithm was demonstrated via analyses on real and synthetic DWI datasets. In addition, the general analytic expression of high order  $b$  matrix is derived in the case of twice refocused spin-echo (TRSE) pulse sequence which is used in the DWI data acquisition. Based on our results, we discuss the benefits of GDT and the second order diffusion tensor on fiber tracking.

**Keywords:** Diffusion tensor imaging, High angular diffusion weighted imaging (HARDI), Human brain, White matter, Tractography

---

\*Technical Report CMIDA-HiPSCCS 009-08, Department of Computer Science, University of Kentucky, KY, 2008.

<sup>†</sup>Laboratory for Computational Medical Imaging & Data Analysis, Department of Computer Science, University of Kentucky, Lexington, KY 40506-0046, USA.

<sup>‡</sup>Department of Anatomy and Neurobiology, MN 214 Chandler Medical Center, University of Kentucky, Lexington, KY, 40536-0298, USA.

<sup>§</sup>MRI/Brain Imaging Physics Group, Institute of Neuroscience and Biophysics-Medicine (INB-3), Research Center Juelich, 52425 Juelich, Germany.

<sup>¶</sup>Laboratory for Computational Medical Imaging & Data Analysis, Department of Computer Science, University of Kentucky, Lexington, KY 40506-0046, USA.

<sup>||</sup>Laboratory for Computational Medical Imaging & Data Analysis, Department of Computer Science, University of Kentucky, Lexington, KY 40506-0046, USA.

<sup>\*\*</sup>The corresponding author. jzhang@cs.uky.edu. Laboratory for Computational Medical Imaging & Data Analysis, Department of Computer Science, University of Kentucky, Lexington, KY 40506-0046, USA.

# 1 Introduction

Diffusion tensor imaging (DTI) tractography has been used in neuroimaging and clinical applications to understand white matter fiber structures of the human brain. However, it has been shown that the second order diffusion tensor model has limitations in resolving complex fiber tracts such as crossing and diverging fibers [44]. Various high angular diffusion weighted imaging (HARDI) techniques have been proposed in an effort to extract more detailed anatomical information via more diffusion weighted imaging (DWI) acquisitions of different angles [4, 10, 13, 14, 19, 41]. Since the spatial voxel size of DTI is limited in the current DWI acquisition techniques, the basic idea of HARDI is to circumvent this spatial limitation by increasing the angular resolution.

One such technique is the generalized diffusion tensor (GDT) imaging [32], [33] which aims to overcome the limitations associated with the standard second order tensor model. Theoretically, the GDT model is more sensitive to the diffusion direction than the second order model when a magnetic field gradient is added. This technique has been demonstrated to be useful in the reconstruction of certain geometrical structures in phantoms by Liu et al. [25]. These authors reconstructed the probability density function (PDF) of the random spin displacement and then described the statistical property of the diffusion process via GDT. The model successfully revealed the underlying geometrical structures which are 3D computer-synthesized phantoms of different typical simple shapes. However, it is not clear how this new model can be used in fiber tractography with human brain datasets.

Anisotropic diffusion simulation methods directly simulate the physical diffusion process of water in the brain tissue. The anisotropic diffusion simulation-based tractography methods [7, 21] improve the reliability of fiber reconstruction of realistic DTI datasets by allowing more than one fiber to emerge from a voxel. This class of methods investigate not only the orientation information carried by the diffusion tensor datasets as most other tracking methods do, but also the influence of the strength of the water diffusion of the diffusion tensor. However, the commonly used second order diffusion tensor model may not contain sufficient information for reconstructing more complex white matter fiber tracts.

In order to make use of the additional diffusion information provided by GDT, we characterize the physical behavior of the diffusion process in the 3D brain volume using the high order tensor datasets. In this study, a new mathematical model is developed which incorporates GDT to anisotropic diffusion simulation. A repeated process of anisotropic diffusion simulation is performed in order to reconstruct the fiber tracts. Furthermore, the relationship between the second order diffusion tensor and the fourth order diffusion tensor is discussed by analyzing the coefficients of the partial differential equation governing the diffusion process.

The diffusion tensor datasets used in the experiment were acquired by using the twice refocused spin-echo (TRSE) diffusion-weighted sequence. This sequence is currently widely used in practice and greatly reduces the atypically large eddy currents generated in the Stejskal-Tanner spin-echo pulse sequence. The existing expression for computing the  $b$  value and  $b$  matrix derived

by Stejskal et al. [38] cannot be applied to this new sequence. To facilitate our computation, a new analytic expression for computing the  $b$  factor and  $b$  matrix of TRSE is also developed by integrating the transverse precessing magnetization during the echo time. The generalized form of the expression is provided.

This paper is organized in the following way. Section 2 is the theoretical part, which describes the generalized diffusion tensor and the diffusion simulation-based fiber tracking algorithm. Section 3 presents the experiments we have conducted. First the computation of the  $b$  matrix is performed. Then several fiber tracking results reconstructed by our algorithm are presented. In Section 4, we discuss the tracking algorithm and the tracking results. The relationship between the second order diffusion tensor and the fourth order diffusion tensor is also discussed in this section. In Section 5, we give a brief concluding remark.

## 2 Theory

### 2.1 DST Algorithm

An anisotropic fluid flow system exhibits a preferential direction while an isotropic system does not have preference [21]. If we use  $C$  to denote the concentration value of water in the human brain that we are modeling, according to Fick's first law, the flux,  $J$ , has magnitude proportional to the concentration gradient,  $\nabla C$ , i.e.,

$$J = d\nabla C,$$

where  $d$  is the diffusion coefficient. Due to the anisotropy of the system under our consideration, the flow field does not follow the gradient of the concentration directly, because the material properties also affect the diffusion and cause diffusion anisotropy [31]. Therefore, the second order diffusion tensor,  $D$ , has been used to better describe the water molecular mobility along each direction and the correlation between these directions. Thus, the flux is given as  $J = D\nabla C$ . One can rewrite the formula in a general way as:

$$J_k = -D_{kl}^{(2)}\nabla_l C - D_{klm}^{(3)}\nabla_{lm} C - D_{klmn}^{(4)}\nabla_{lmn} C - \dots, \quad (1)$$

where  $k, l, m, n = (x, y, z)$  are the dimension indices of the 3D space and  $D^{(n)}$  is the  $n$ -th order diffusion coefficient. In this paper, the Einstein notation is used for expressing the equations [12]. According to the notation, when an index variable appears twice in a single term, it implies that we are summing over all of its possible values. Also, the partial derivatives in Eq. (1) were written as:

$$\nabla_{i_1 i_2 \dots i_n} = \frac{\partial^n}{\partial_{i_1} \partial_{i_2} \dots \partial_{i_n}}. \quad (2)$$

From the continuity equation which expresses the conservation of the mass, the generalized partial differential equation (PDE) governing the diffusion process can be written as [25]:

$$\begin{aligned}\frac{\partial C}{\partial t} &= -\nabla_k J_k \\ &= \nabla_k (D_{kl}^{(2)} \nabla_l C + D_{klm}^{(3)} \nabla_{lm} C + D_{klmn}^{(4)} \nabla_{lmn} C + \dots).\end{aligned}\quad (3)$$

In the description above, the  $n$ -th order diffusion tensor  $D^{(n)}$  is the diffusion coefficient, which fully characterizes the motion of water in all directions. The  $n$ -th order diffusion tensor is an  $n$ -th dimensional symmetric array, which has  $3^n$  elements. Due to the symmetry of the tensor, all the permutation of  $i_1 i_2 i_3 \dots i_n$  which is the subscript of  $D_{i_1 i_2 i_3 \dots i_n}^{(n)}$  have the same value, for example,  $D_{xxx \dots xy}^{(n)} = D_{xx \dots yx}^{(n)}$ .

## 2.2 Computation of High Order Tensors

In his classic work devoted to spin echoes, Hahn showed that diffusion in a nonuniform magnetic field contributes to decay of the transverse magnetization in media [16]. To analyze the effect of diffusion, we start with the equation that describes the dynamics of magnetization due to self-diffusion of particles in isotropic homogeneous media [37]:

$$\frac{\partial M_{xy}}{\partial t} = D_{kl}^{(2)} \nabla_{kl} M_{xy}, \quad (4)$$

where  $M_{xy}$  is the transverse magnetization,  $D$  is the diffusion coefficient. Torrey [40] demonstrated that in order to incorporate the effects of T1 and T2 relaxations and precession in an external magnetic field, the corresponding terms from the Bloch equations can be added to the right-hand side of Eq. (4). Below we will derive an exact solution of the Bloch equations in the case when diffusion of spins occurs in the presence of linear magnetic field gradients.

A nonuniform magnetic field  $B$  is given by a sum of constant and linear terms:

$$B = k(B_0 + \mathbf{G} \cdot \mathbf{r}). \quad (5)$$

Here  $\mathbf{G}$  is the magnetic field gradient and  $\mathbf{r}$  is the radio frequency field. The dynamics of magnetization in the rotating reference frame can be described by the modified Bloch equations [38]:

$$\frac{\partial M_{xy}}{\partial t} = -\frac{M_{xy}}{T_2} - i\gamma \mathbf{G} \cdot \mathbf{r} M_{xy} + D_{kl}^{(2)} \nabla_{kl} M_{xy}, \quad (6)$$

where  $\gamma$  is the gyromagnetic ratio. Introducing  $\psi(\mathbf{r}, t)$  through  $M_{xy} = \psi e^{(i\omega_0 t - \frac{t}{T_2})}$  into Eq. (6), we have

$$\frac{\partial \psi}{\partial t} = -i\gamma (\mathbf{G} \cdot \mathbf{r}) \psi + D \nabla^2 \psi. \quad (7)$$

The solution of  $\psi$  in Eq. (7) is in the form of

$$\psi = A e^{(-i\gamma F(\mathbf{G}, t) \mathbf{r})}.$$

Note that  $F(\mathbf{G}, t)$  is the function of  $\mathbf{G}$  and time  $t$ . Taking into account the diffusion term by assuming that  $A$  is a function of the time only, then Eq. (7) yields:

$$\frac{dA}{dt} = -\gamma^2 (F(\mathbf{G}, t))^2 D^{(2)} A. \quad (8)$$

Integrating Eq. (8) between  $t = 0$  and  $t = \text{TE}$  (the echo time), we have:

$$\ln \left( \frac{A}{A_0} \right) = - \left( \int_0^{\text{TE}} \gamma^2 (F(\mathbf{G}, t))^2 dt \right) D^{(2)}. \quad (9)$$

Here,  $A_0$  is proportional to the transverse magnetization at the time before the first  $90^\circ$  radio frequency pulse, which is the unweighted echo signal.  $A$  is proportional to the transverse magnetization after the echo time (TE), which is corresponding to the weighted signal. For our generalization purpose, the generalized form of the Eq. (6) can be written as [25]:

$$\frac{\partial M_{xy}}{\partial t} = -\frac{M_{xy}}{T_2} - i\gamma \mathbf{G} \cdot \mathbf{r} M_{xy} + D_{kl}^{(2)} \nabla_{kl} M_{xy} + D_{klm}^{(3)} \nabla_{lm} C + D_{klmn}^{(4)} \nabla_{lmn} C + \dots \quad (10)$$

We can rewrite Eq. (10) in the form of standard diffusion-weighted image acquisition for tensor estimation as [25]:

$$\begin{aligned} \ln \left( \frac{A}{A_0} \right) = & -b_{i_1 i_2}^{(2)} D_{i_1 i_2}^{(2)} + b_{i_1 i_2 i_3 i_4}^{(4)} D_{i_1 i_2 i_3 i_4}^{(4)} - \dots + (-1)^n b_{i_1 i_2 \dots i_{2n}}^{(2n)} D_{i_1 i_2 \dots i_{2n}}^{(2n)} + \dots \\ & - \mathbf{j} (b_{i_1 i_2 i_3}^{(3)} D_{i_1 i_2 i_3}^{(3)} - b_{i_1 i_2 i_3 i_4 i_5}^{(5)} D_{i_1 i_2 i_3 i_4 i_5}^{(5)} - \dots - (-1)^{n+1} b_{i_1 i_2 \dots i_{2n+1}}^{(2n+1)} D_{i_1 i_2 \dots i_{2n+1}}^{(2n+1)} - \dots). \end{aligned} \quad (11)$$

In the generalized diffusion simulation-based tracking algorithm, we used the fourth order diffusion tensor as well as the second order diffusion tensor in order to improve the tracking sensitivity, as the third order diffusion tensor may represent noise [13]. Because the computation is in the real domain and the order of the diffusion tensor used in the algorithm is the second and the fourth orders, the imaginary terms and the real terms whose orders are greater than four are not necessary, so they are truncated. The modified generalized diffusion tensor equation (11) can thus be written as:

$$\ln \left( \frac{A}{A_0} \right) = -b_{i_1 i_2}^{(2)} D_{i_1 i_2}^{(2)} + b_{i_1 i_2 i_3 i_4}^{(4)} D_{i_1 i_2 i_3 i_4}^{(4)} \quad (12)$$

Although the  $b$  value for the second order tensor,  $b_{i_1 i_2}^{(2)}$ , can be obtained from the MRI machine, the fourth order  $b$  value,  $b_{i_1 i_2 i_3 i_4}$ , is not generally available. So the fourth order  $b$  value needs to be computed (see Appendix for a detailed computation procedure for  $b$ ).

After computing the  $b$  value, a linear system for computing the generalized diffusion tensor

can be built, based on Eq. (12), as,

$$\begin{bmatrix} -b_{11}^1 & -b_{12}^1 & \cdots & -b_{33}^1 & b_{1111}^1 & b_{1112}^1 & \cdots & b_{3333}^1 \\ -b_{11}^2 & -b_{12}^2 & \cdots & -b_{33}^2 & b_{1111}^2 & b_{1112}^2 & \cdots & b_{3333}^2 \\ \vdots & \vdots & \ddots & \vdots & \vdots & \vdots & \ddots & \vdots \\ -b_{11}^n & -b_{12}^n & \cdots & -b_{33}^n & b_{1111}^n & b_{1112}^n & \cdots & b_{3333}^n \end{bmatrix} \begin{bmatrix} D_{11} \\ D_{12} \\ \vdots \\ D_{33} \\ D_{1111} \\ D_{1112} \\ \vdots \\ D_{3333} \end{bmatrix} = \begin{bmatrix} \ln(S_1/S_0) \\ \ln(S_2/S_0) \\ \vdots \\ \ln(S_n/S_0) \end{bmatrix} \quad (13)$$

Due to the characteristics of the symmetry of the diffusion tensor, it is easy to see that: 6 different angles of magnetic-field gradients are needed in order to get 6 different ratios of weighted and unweighted signals for the second order tensor computation. 15 different angles of gradients are needed for the fourth order tensor computation. So in total, 21 different DWIs are needed for computing the second and fourth order tensors.

### 2.3 Generalized Diffusion Simulation Based Tractography (GDST)

Return to Eq. (3), after the computation of the high order diffusion tensor, the generalized diffusion process in the PDE Eq. (3) can be written as:

$$\frac{\partial C}{\partial t} = \frac{\partial J_1}{\partial x} + \frac{\partial J_2}{\partial y} + \frac{\partial J_3}{\partial z}, \quad (14)$$

where

$$\begin{aligned} J_1 = & - \left( D_{xx} \frac{\partial C}{\partial x} + D_{xy} \frac{\partial C}{\partial y} + D_{xz} \frac{\partial C}{\partial z} + D_{xxxx} \frac{\partial^3 C}{\partial x^3} + 3D_{xxxy} \frac{\partial^3 C}{\partial x^2 \partial y} + 3D_{xxxz} \frac{\partial^3 C}{\partial x^2 \partial z} \right. \\ & + 3D_{xxyy} \frac{\partial^3 C}{\partial x \partial y^2} + 6D_{xyyz} \frac{\partial^3 C}{\partial x \partial y \partial z} + 3D_{xxzz} \frac{\partial^3 C}{\partial x \partial z^2} + D_{yyyy} \frac{\partial^3 C}{\partial y^3} + 3D_{xyyz} \frac{\partial^3 C}{\partial y^2 \partial z} \\ & \left. + 3D_{xyzz} \frac{\partial^3 C}{\partial y \partial z^2} + D_{zzzz} \frac{\partial^3 C}{\partial z^3} \right), \end{aligned}$$

$$\begin{aligned} J_2 = & - \left( D_{yx} \frac{\partial C}{\partial x} + D_{yy} \frac{\partial C}{\partial y} + D_{yz} \frac{\partial C}{\partial z} + D_{yxxx} \frac{\partial^3 C}{\partial x^3} + 3D_{yxyx} \frac{\partial^3 C}{\partial x^2 \partial y} + 3D_{yxxz} \frac{\partial^3 C}{\partial x^2 \partial z} \right. \\ & + 3D_{yxyy} \frac{\partial^3 C}{\partial x \partial y^2} + 6D_{yxyz} \frac{\partial^3 C}{\partial x \partial y \partial z} + 3D_{yxzz} \frac{\partial^3 C}{\partial x \partial z^2} + D_{yyyy} \frac{\partial^3 C}{\partial y^3} + 3D_{yxyz} \frac{\partial^3 C}{\partial y^2 \partial z} \\ & \left. + 3D_{yzzz} \frac{\partial^3 C}{\partial y \partial z^2} + D_{zzzz} \frac{\partial^3 C}{\partial z^3} \right), \end{aligned}$$

$$\begin{aligned}
J_3 = & - \left( D_{zx} \frac{\partial C}{\partial x} + D_{zy} \frac{\partial C}{\partial y} + D_{zz} \frac{\partial C}{\partial z} + D_{zxxx} \frac{\partial^3 C}{\partial x^3} + 3D_{zxy} \frac{\partial^3 C}{\partial x^2 \partial y} + 3D_{zxxz} \frac{\partial^3 C}{\partial x^2 \partial z} \right. \\
& + 3D_{zyyy} \frac{\partial^3 C}{\partial x \partial y^2} + 6D_{zyyz} \frac{\partial^3 C}{\partial x \partial y \partial z} + 3D_{zxxx} \frac{\partial^3 C}{\partial x \partial z^2} + D_{zyyy} \frac{\partial^3 C}{\partial y^3} + 3D_{zyyz} \frac{\partial^3 C}{\partial y^2 \partial z} \\
& \left. + 3D_{zyzz} \frac{\partial^3 C}{\partial y \partial z^2} + D_{zzzz} \frac{\partial^3 C}{\partial z^3} \right).
\end{aligned}$$

To seek a numerical solution of Eq. (14), the PDE is discretized by using the central difference scheme, and the discretized system is solved by using the biconjugate gradients stabilized (BiCGSTAB) Krylov subspace method [43] with an incomplete LU (Lower-Upper) factorization preconditioner [28]. For computational efficiency, we restrict our simulation in a diffusion kernel which is a cubic space inside the brain. For the boundary condition, the diffusion kernel is considered as an insulated cube where no water can diffuse out of it. So we write the boundary condition for Eq. (14) as [35]:

$$\frac{\partial \rho}{\partial k} = \hat{n} \cdot \nabla \rho = 0. \quad (15)$$

Here  $k$  can be  $x$ ,  $y$  or  $z$  and  $\hat{n}$  is the outward-pointing vector normal to the boundary. After the time integration for solving Eq. (14), a discrete approximation to the diffusion front is calculated to determine whether the concentration value in a voxel is zero. Thus all discrete node voxels in the diffusion kernel can be partitioned into two groups, one with zero concentration value and the other with nonzero values. The diffusion front is the set of nodes (voxels) with nonzero concentration value, but have neighboring nodes with zero concentration value. A few nodes can be picked up from the diffusion front and used as the root nodes for the next phase of the diffusion simulation with different diffusion kernels. These nodes are usually the furthest ones away from the previous seed node, indicating that the diffusion is fastest along those directions.

This successive diffusion procedure can be continued until the termination conditions shown in Figure 1 are met. A back propagation from the voxels on the diffusion fronts by following continuously the corresponding predecessor voxels leads to paths that merge to the starting voxel and form a fiber tract. One or more fiber tracts can be reconstructed from a given seed node by using this procedure.

Figure 1 illustrates the method for choosing the successive diffusion seeds: the blue dot is the initial diffusion seed, red dots are on the chosen diffusion front, the tubes connecting them are the reconstructed fibers. The diffusion front nodes can be selected by defining proper values of the two thresholds: (1) the angle  $\alpha$  between the vectors which are formed by connecting the nodes one by one from the root; (2) the fractional anisotropy (FA) value of the nodes [5]. The angle is usually selected between  $\pi/4$  and  $\pi/3$  in order to make the constructed fiber grow forward instead of backward, and the fractional anisotropy value is usually selected at the value 0.3-0.1 to make sure that the reconstructed tract stays in the white matter area. The reason for selecting the fractional anisotropy as one of the stopping criteria is that the fractional anisotropy will help control the diffusion process to take place in a reasonable range inside of the brain. After the diffusion voxels are selected, the fiber pathways from the original diffusion seed voxel

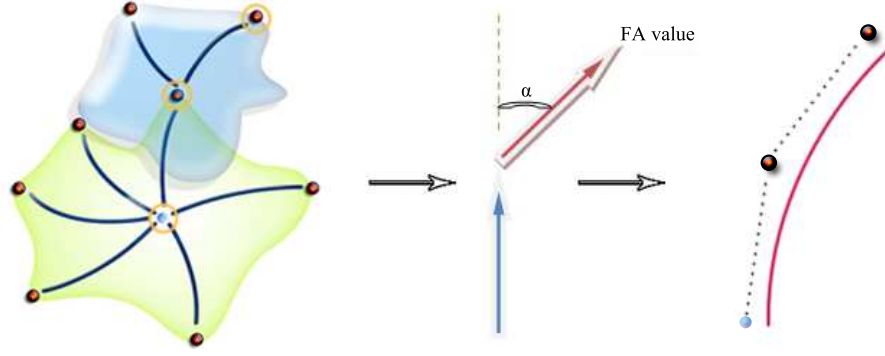


Figure 1: Diffusion simulation and the stopping criteria. The green region illustrates the first step of the diffusion. After some diffusion fronts are chosen by the criteria of the angle and the FA value, another diffusion process is performed in the blue region, in which one of the diffusion front voxels from the last diffusion phase is chosen as the new seed point. Three circled points are selected for constructing a fiber path. The two criteria of the selection are shown in the middle. After the voxels on the fiber pathway is selected, a Bézier curve interpolation is applied to the pathway in order to make the fiber smoother. The interpolated curve is shown on the right.

to all the leaf voxels are connected. Then a Bézier interpolation is applied to the neighboring voxels along all the fiber pathways. Smoother fiber tracts can be produced by the interpolation.

## 3 Results

### 3.1 Computation of the $\mathbf{b}$ matrix

The diffusion tensor data were obtained from a 1.5 T Siemens Sonata MR scanner. The scanning process used the following parameters: TE = 96 ms, TR = 5000 ms, voxel size: 2.0 mm  $\times$  2.0 mm  $\times$  2.2 mm, field of view (FOV)=256 mm. The gyromagnetic ratio  $\gamma/2\pi = 42.57$  MHz/T. The data were scanned with the twice-refocused spin echo diffusion weighted sequence, which is shown in Figure 10 in the Appendix. Using one diffusion gradient direction (1, 0, 1) as an example, the magnetic gradients are 23.3664 mT/m on the  $x$  axis, 0 mT/m on the  $y$  axis and 23.3664 mT/m on the  $z$  axis. In the sequence, it is estimated that  $t_1 = 27.15$  ms,  $t_2 = 37.3$  ms,  $t_3 = 59$  ms,  $t_4 = 85.25$  ms,  $\delta_1 = 5.0$  ms,  $\delta_2 = 22.0$  ms,  $\delta_3 = 21.5$  ms,  $\delta_4 = 5.4$  ms, see the Appendix for the meaning of these parameters. The computed second order  $b$  value according to Eq. (24) is 1046.4 s/mm<sup>2</sup>, while the real second order  $b$  value read from the machine is 1000 s/mm<sup>2</sup>, so the relative error between the computed one and the real one is 5%. Given the fact that several parameters used in the computation were estimated, this 5% relative error can be seen as small. The second order  $b$  matrix computed by the given  $b$  value and the second order  $b$  matrix computed by Eq. (24) are shown in Tables 1 and 2.

The fourth order  $b$  matrix is not available from the MRI scanner. We therefore have to use

Table 1: The 2nd order  $b$  matrix from a given  $b$  value. Unit:  $\text{s}/\text{mm}^2$ .

$\vec{g}$	$(-0.11, 0.66, 0.74)$			$(-0.86, 0.50, 0.02)$		
$b = 1000$	$g_x$	$g_y$	$g_z$	$g_x$	$g_y$	$g_z$
$g_x$	12.1	-72.6	-81.4	739.6	-430.0	17.2
$g_y$	-72.6	435.6	488.4	-430.0	250.0	10.0
$g_z$	-81.4	488.4	547.6	17.2	10.0	0.4

Table 2: The 2nd order  $b$  matrix from computation. Unit:  $\text{s}/\text{mm}^2$ .

$\vec{g}$	$(-0.11, 0.66, 0.74)$			$(-0.86, 0.50, 0.02)$		
$b = 1046$	$g_x$	$g_y$	$g_z$	$g_x$	$g_y$	$g_z$
$g_x$	12.6	-75.9	-85.1	773.9	-450.0	18.1
$g_y$	-75.9	455.8	511.0	-450.0	261.6	10.5
$g_z$	-85.1	511.0	573.0	18.1	10.5	0.4

the analytic formula for  $b$ , Eq. (24), to compute the fourth order  $b$  matrix. As an example, Table 3 lists the results for one diffusion gradient direction  $(-0.11, 0.66, 0.74)$ .

### 3.2 Synthetic dataset

The first tracking experiment was conducted by using the GDST algorithm to perform the fiber tracking on several synthetic diffusion tensor datasets. By tracking the synthetic data with known fibers, the correctness and the robustness of the algorithm can be determined. This set of the synthetic data is a group of helices in a  $50 \times 50 \times 20$  space.

Figures 2 and 3 show the reconstructed helix tracts from the synthetic dataset: the four individual helices. Figure 2 shows the perspective view in the 3D space; Figure 3 shows the transverse view on the XY plane of the reconstructed tracks. The red dots represent the starting seed points of the tracking processes. The tracking result shows that the four individual helices were reconstructed without any mixing between one and another.

Table 3: Computed data of the 4th order  $b$  matrix. Unit:  $\text{s}/\text{mm}^4$ .

$\vec{g} = (-0.11, 0.66, 0.74)$					
	value		value		value
$b_{xxxx}$	$5.14 \times 10^3$	$b_{xxyz}$	$2.07 \times 10^5$	$b_{xyyy}$	$-1.11 \times 10^6$
$b_{yyyy}$	$6.66 \times 10^6$	$b_{xyyy}$	$1.85 \times 10^5$	$b_{yyyz}$	$7.46 \times 10^6$
$b_{zzzz}$	$1.05 \times 10^7$	$b_{xyyz}$	$-1.24 \times 10^6$	$b_{yyzz}$	$8.37 \times 10^6$
$b_{xxxy}$	$-3.08 \times 10^4$	$b_{xxzz}$	$2.32 \times 10^5$	$b_{xzzz}$	$-1.56 \times 10^6$
$b_{xxxz}$	$-3.54 \times 10^4$	$b_{xyzz}$	$-1.39 \times 10^6$	$b_{yzzz}$	$9.38 \times 10^6$

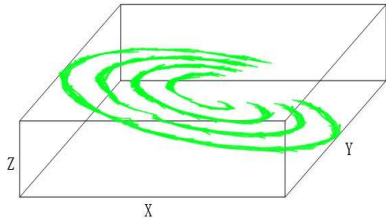


Figure 2: 3D view of the reconstructed synthetic helix tracts.

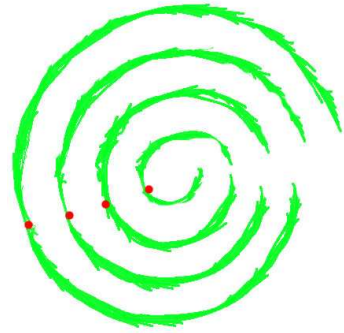


Figure 3: X-Y plane view of the reconstructed synthetic helix tracts, the red dots are the starting points.

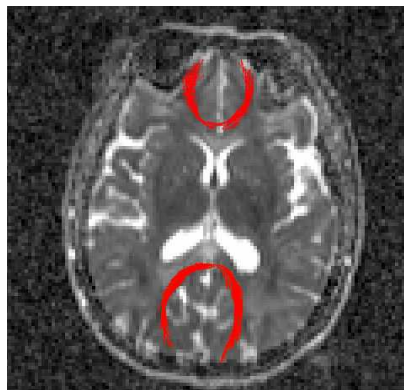


Figure 4: Axial view of the reconstructed fiber tracts passing through the genu (front of figure) and splenium (back of figure) of the corpus callosum.

### 3.3 In vivo datasets

As mentioned above, the in vivo diffusion weighted MR images were obtained from a healthy subject. The DWI dataset contains 21 volume images with  $b = 1000$  and one volume image with  $b = 0$ . They were used to compute the second and fourth order tensors. We now present reconstructions of some typical fiber tracts.

A tracking of the corpus callosum was performed. Figure 4 shows the fiber tracts computed from two starting regions of interest (ROIs) selected in the genu and the splenium of the corpus callosum [3, 15, 11], respectively. The genu is the anterior part of the corpus callosum. It courses forward and downward in front of the septum pellucidum, terminating in the rostrum. The splenium is the posterior and thickest part of the corpus callosum [18]. The trackings began separately at two seed points, and each seed point was in the middle of one fiber path. The result in an axial view shows that the two fiber paths are correctly reconstructed.

A tracking of a fiber intersection was examined as well. The tracking experiment was con-

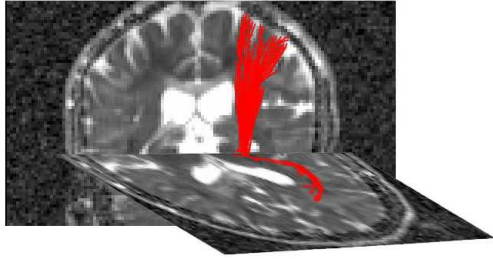


Figure 5: Reconstructed corticospinal tract in a coronal view and optic radiation tracts in an axial view.

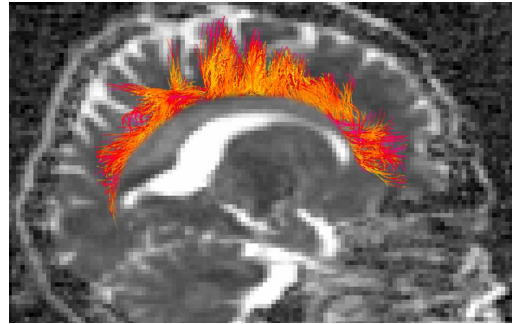


Figure 6: Visualization of the commissural fibers crossing the corpus callosum, in a sagittal view.

ducted to see if some neighboring fiber tracts could be found. A seed point in the middle of the corticospinal tract was selected [11, 17, 23, 24, 30, 39]. The corticospinal tract is a massive collection of axons that travels between the cerebral cortex of the brain and the spinal cord, and it mostly consists of motor axons. Figure 5 shows the corticospinal tracts and a part of the optic radiation. The corticospinal tract is presented in the coronal view and the optic radiation tract is presented in a transverse view. This result shows that our algorithm can track branching fibers. It is also possible that a small number of spurious fibers may have been reconstructed.

A tracking was then performed around the corpus callosum [20, 17] by choosing a ROI across the corpus callosum. Several voxels over the lateral ventricle were selected as the seed points for the tracking. Figure 6 shows the result of the tracking. The reconstructed commissural fibers connect the two hemispheres. It can be seen in the figure that the anterior part corresponds to the coronal radiata. This part of the tract courses upward along the lateral ventricle, which is in accord with the known human brain anatomy [18].

The tracking results from Figure 4 to Figure 6 demonstrate that the generalized diffusion simulation tractography algorithm used in the tracking experiments above is able to reconstruct similar fiber tracts as the standard diffusion simulation algorithm [21] on the tracking of typical fiber bundles.

Finally, we compared the tracking results derived from the second order diffusion tensor and the generalized diffusion tensor. The fiber tracking from the second order diffusion tensor was performed by turning off the fourth order diffusion tensor terms in the generalized diffusion tensor used in our GDST algorithm. The fiber tracts across the middle temporal gyrus and the middle occipital gyrus were chosen as the first experiment for the comparison. The seed point was selected below the insula. The results are shown in Figure 7.

A fiber tracking of the inferior fronto occipital fasciculus was then selected as the second experiment for the comparison, see Figure 8. The seed point was selected in the posterior part of the brain. The difference between the second order diffusion tensor tracking (green) and the generalized diffusion tensor tracking (red) can be seen from two groups of magnified fiber tracts in Figure 7 and Figure 8: (1) the red fiber tract shows more and longer fibers than the green

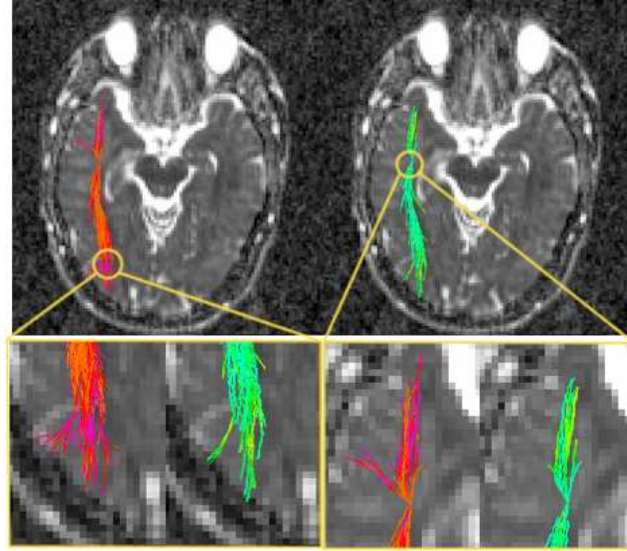


Figure 7: Comparisons of the tracts across the middle temporal gyrus and the middle occipital gyrus reconstructed separately by the second order tensor and the generalized tensor. The green fibers were reconstructed by the second order tensor only; the red fibers were reconstructed by the generalized tensor.

one; (2) the red fiber tract has more secondary fiber branches than the green one.

## 4 Discussion

A high order generalized diffusion simulation-based fiber tracking algorithm was proposed and implemented. Several well-known fiber bundles in different regions of the human brain were reconstructed and compared. In the algorithm, we first proposed an analytic  $b$  value expression for the TRSE pulse sequence, and used the formula to compute the high order  $b$  matrix and then computed the high order diffusion tensor for the in vivo DWI datasets. The formula is useful in the high order diffusion tensor computation and visualization while the use of the TRSE image is popular nowadays.

The anisotropic diffusion simulation was performed by solving the governing partial differential equation using an iterative method. Several tracking experiments were conducted after the analytic computation of the  $b$  value and the diffusion tensor. In the experiments, synthetic datasets and clinical datasets were tracked separately. The corpus callosum, corticospinal tracts, optic radiation and coronal radiata were reconstructed in the experiment. The comparison of the second order tensor fiber tracking and the generalized tensor fiber tracking was performed by implementing a tracking in two fiber bundles: one is the fiber bundle across the middle temporal gyrus and the middle occipital gyrus, the other is the inferior fronto occipital fasciculus fiber

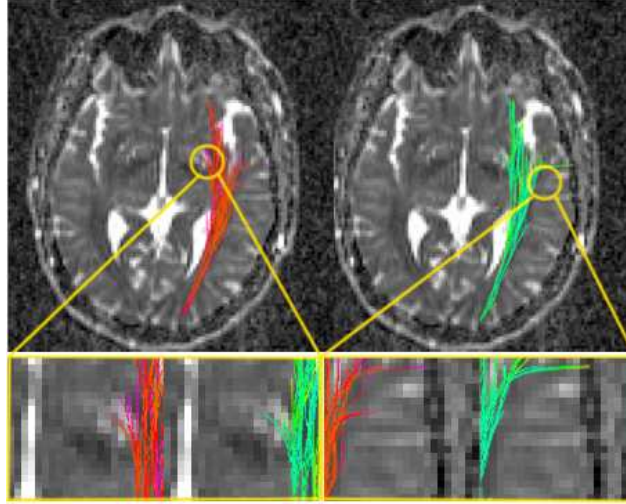


Figure 8: Comparisons of the inferior fronto occipital fasciculus tracts reconstructed separately by the second order tensor and the generalized tensor. The green fibers were reconstructed by the second order tensor only; the red fibers were reconstructed by the generalized tensor.

bundle. The results showed that it is feasible to combine the diffusion simulation with the high order generalized diffusion tensor model in order to reconstruct complex fiber tracts.

From the second order  $b$  value computation in Eq. (24) we know that: when the standard unit,  $s/m^2$ , is used, the amount of the fourth order  $b$  value is about the square of the second order  $b$  value. Suppose that one of the second order  $b$  values in the second order  $b$  matrix is equal to  $k$   $s/m^2$ , the fourth order  $b$  values are about the square of the second order  $b$  values, that is  $k^2$   $s/m^4$ , so they are much greater than the second order  $b$ . Then in the linear system Eq. (13) of the diffusion simulation equation which has a right-hand side in the form of  $[0, 0, \dots, 0, 1, 0, \dots, 0]^T$ , we can solve the second order tensor  $D^{(2)}$  which is about  $1/k$   $m^2/s$ , and the fourth order tensor  $D^{(4)}$  which is about  $1/k^2$   $m^4/s$ . We can see that the fourth order  $b$  value is much greater than the second order  $b$  value while the fourth order tensor is much smaller than the second order tensor. In the final diffusion simulation PDE, the coefficient with the second order tensor is like:

$$\frac{D^{(2)}}{dx^2}, \quad (16)$$

where  $dx$  can also be  $dy$  or  $dz$ . The coefficient with the fourth order tensor is like:

$$\frac{D^{(4)}}{dx^4}. \quad (17)$$

The ratio of Eq. (16) to Eq. (17) is:

$$\frac{D^{(2)}}{dx^2} / \frac{D^{(4)}}{dx^4} = \frac{D^{(2)} \cdot dx^2}{D^{(4)}} \approx k \cdot dx^2. \quad (18)$$

The unit of  $dx$ ,  $dy$  and  $dz$  used in our current study is millimeter, so the final effect of the fourth order tensor on the tracking results depends on how large the chosen spatial mesh size  $dx$ ,  $dy$  and  $dz$  is. Usually, the spatial step, which is related to the voxel size, is chosen as  $1 \times 10^{-3}$  m. Thus the effect of the coefficients with the fourth order tensor is  $k \times 10^{-6}$  times smaller than the coefficients with the second order tensor. On the other hand, suppose we select a smaller spatial step, say,  $dx = 1/\sqrt{k}$ , Eq. (18) is approximately equal to 1, which means the effect of the coefficients with the fourth order tensor is approximately the same as that of the coefficients with the second order tensor. For example, if we select a second order  $b$  value of  $1000$  s/mm<sup>2</sup>, that is  $10^9$  s/m<sup>2</sup> in standard unit, so the fourth order tensor will have approximately the same effect as the second order tensor when a spatial mesh size  $dx = dy = dz \approx 10^{-4.5}$  m is selected. So the effect of the fourth order tensor on the tracking results is related to how to choose the spatial step length for solving the diffusion simulation PDE. A balance of the second order tensor and the fourth order tensor could be achieved by selecting the appropriate spatial parameters for solving the diffusion simulation PDE.

This analysis also shows that the effect of the high order tensor will become more important when the MRI machine is able to produce higher spatial resolution diffusion weighted imaging data. Thus, we anticipate a promising future use of the high order diffusion tensor methods in fiber tractography as the MRI techniques improve.

## 5 Conclusion

A new fiber tracking algorithm combining the generalized diffusion tensor and diffusion simulation, the generalized diffusion simulation algorithm, has been developed in this paper. The new algorithm was used to reconstruct complex white matter fiber tracts in the human brain. From the experiment we showed that the algorithm is able to reconstruct several main white matter fiber bundles. It is more sensitive to model complex white matter fiber tracts than the standard diffusion simulation-based tracking algorithm due to the use of the fourth order diffusion tensor terms. Because the real datasets used in the experiment were scanned by the TRSE pulse sequence, a new analytic expression for computing the  $b$  value of generalized diffusion tensor for the TRSE datasets was proposed. The relationship between the second order tensor tracking and the fourth order tensor tracking was analyzed. In summary, the generalized diffusion simulation algorithm is a diffusion simulation-based fiber tracking algorithm with the high order diffusion tensor as the diffusion coefficients. The algorithm can be used to reconstruct certain complex white matter fiber tracks.

## Acknowledgements

The authors would like to thank Dr. C. Liu for useful discussions during the early phase of this study.

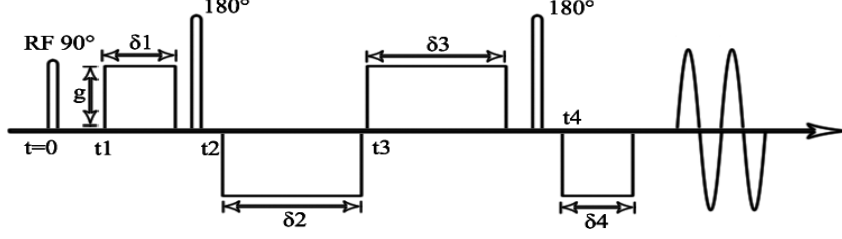


Figure 9: Twice refocused spin-echo (TRSE) pulse sequence.  $\delta_1$  to  $\delta_4$  are the duration time of the magnetic field gradients;  $t_1$  to  $t_4$  are the starting time of the magnetic field gradients.  $g$  is the actual magnetic field gradient strength.

## Appendix

### The analytic expression for the $b$ matrix

We can first obtain the generalized form of Eq. (9) as:

$$\ln\left(\frac{A}{A_0}\right) = -\int_0^{TE} \gamma^2 (F(\mathbf{G}, t))^2 dt D^{(2)} + \int_0^{TE} \gamma^4 (F(\mathbf{G}, t))^4 dt D^{(4)}. \quad (19)$$

The Stejskal-Tanner spin-echo (STSE) sequence was once commonly used, and many spin-echo (SE) sequence variants have been created based on that sequence [26]. However, the STSE is vulnerable to the eddy current effect because of the large gradient pulse used. Image distortion due to field gradient eddy currents can create image artifacts in diffusion-weighted MR images. Several methods have been proposed [2, 8] to minimize the eddy current effect. One of them is the twice refocused spin-echo (TRSE) sequence presented by Reese [34]. By changing the design of the pulse sequence, the TRSE sequence uses the strategy which compensates the eddy currents by applying on and off field gradient transactions to produce equal and opposite eddy currents in order to null eddy currents. The TRSE sequence is shown in Figure 9 with:

$$\delta_1 + \delta_2 = \delta_3 + \delta_4, \quad \delta_2 + \delta_3 = TE/2, \quad \delta_1 + \delta_4 = TE/2 - t_{pr}. \quad (20)$$

Here  $\delta_1$  to  $\delta_4$  are the time durations of the magnetic field gradient,  $t_1$  to  $t_4$  are the starting time of the magnetic field gradient pulse and  $t_{pr}$  is the sum of the preparation time following the excitation pulse and the readout time preceding the spin echo sequence [34]. Based on the TRSE sequence, the value of  $b$  can be computed analytically. Because the TE is fixed during one scanning and  $\gamma$  is the gyromagnetic ratio of the hydrogen which is a constant value, the change of the  $b$  value is only dependent on  $F(\mathbf{G}, t)$ . According to the illustration of the TRSE in Figure 9, the  $b$  value can be calculated in three parts. Between the 90° RF pulse and the first 180° RF pulse,  $F_0(\mathbf{G}, t)$  can be calculated as follows:

$$F_0(G, t) = \int_0^t G(t') dt'. \quad (21)$$

Table 4: Change of magnetic field gradient at different time.

Time $t$	Diffusion gradient
0 to $t_1$	0
$t_1$ to $t_1 + \delta_1$	$g$
$t_1 + \delta_1$ to $t_2$	0
$t_2$ to $t_2 + \delta_2$	$-g$
$t_3$ to $t_3 + \delta_3$	$g$
$t_3 + \delta_3$ to $t_4$	0
$t_4$ to $t_4 + \delta_4$	$-g$
$t_4 + \delta_4$ to $TE$	0

By the principle of spin-echo, the effect of the first  $180^\circ$  RF pulse is to set back the phase of precessing magnetization at each point by twice the angle  $\alpha = -\gamma(\mathbf{Gr})\tau$  through which it has advanced during the time  $\tau$ , where  $\tau$  is the time elapsed from  $90^\circ$  RF pulse to the first  $180^\circ$  RF pulse [1]. So according to the above description, between the first  $180^\circ$  RF pulse and the second  $180^\circ$  RF pulse, we have the  $F_1(G, t)$  as:

$$F_1(G, t) = F_0(G, t) - 2F_0(G, \tau). \quad (22)$$

The effect of the second  $180^\circ$  RF pulse is the same as the first one. Suppose the second  $180^\circ$  RF pulse happens at the time  $\tau'$ , then the  $F(G, t)$  function for this period is:

$$F_2(G, t) = F_1(G, t) - 2F_1(G, \tau'). \quad (23)$$

The change of  $G(t')$  with respect to different time can be found according to Table 4 which shows the relationship between time and magnetic field gradient illustrated in Figure 9.

For the  $n$ -th order tensor:  $b = \int_0^{TE} \gamma^n (F(G, t))^n dt$ , integrating the right-hand side using the values in Table 4, we get the results of  $F$  in Table 5.

So the  $n$ -th order  $b$  value for the TRSE can be expressed as:

$$b = -\frac{1}{n+1} \gamma^n g^n [2(\delta_1 + \delta_2)^{n+1} + (\delta_3 + \delta_4 - \delta_1 - \delta_2)^{n+1}] - \gamma^n g^n [\delta_1^n (t_2 - t_1 - \delta_1) + (\delta_3 - \delta_1 - \delta_2)^n (t_4 - t_3 - \delta_3)], \quad (24)$$

and the element in the  $b$  matrix is:

$$b_{i_1 i_2 \dots i_n} = -\frac{1}{n+1} \gamma^n g_{i_1} g_{i_2} \dots g_{i_n} [2(\delta_1 + \delta_2)^{n+1} + (\delta_3 + \delta_4 - \delta_1 - \delta_2)^{n+1}] - \gamma^n g_{i_1} g_{i_2} \dots g_{i_n} [\delta_1^n (t_2 - t_1 - \delta_1) + (\delta_3 - \delta_1 - \delta_2)^n (t_4 - t_3 - \delta_3)].$$

The RF and the  $x$  axis gradient pulse sequence that we got directly from the MRI machine is shown in Figure 10, in which the magnetic gradients are 23.3664 mT/m on the  $x$  and  $z$  axis, 0 mT/m on the  $y$  axis.

Table 5: Computed result of the function  $F(G, t)$ .

Time $t$	$F(G, t)$
0 to $t_1$	0
$t_1$ to $t_1 + \delta_1$	$-\frac{1}{n+1}\gamma^n g^n \delta_1^{n+1}$
$t_1 + \delta_1$ to $t_2$	$-\gamma^n g^n \delta_1^n (t_2 - t_1 - \delta_1)$
$t_2$ to $t_2 + \delta_2$	$-\frac{1}{n+1}\gamma^n g^n ((\delta_1 + \delta_2)^{n+1} - \delta_1^{n+1})$
$t_3$ to $t_3 + \delta_3$	$-\frac{1}{n+1}\gamma^n g^n ((\delta_3 - \delta_1 - \delta_2)^{n+1} + (\delta_1 + \delta_2)^{n+1})$
$t_3 + \delta_3$ to $t_4$	$-\gamma^n g^n (\delta_1 + \delta_2 - \delta_3)^n (t_4 - t_3 - \delta_3)$
$t_4$ to $t_4 + \delta_4$	$-\frac{1}{n+1}\gamma^n g^n ((\delta_3 + \delta_4 - \delta_1 - \delta_2)^{n+1} - (\delta_3 - \delta_1 - \delta_2)^{n+1})$
$t_4 + \delta_4$ to TE	0

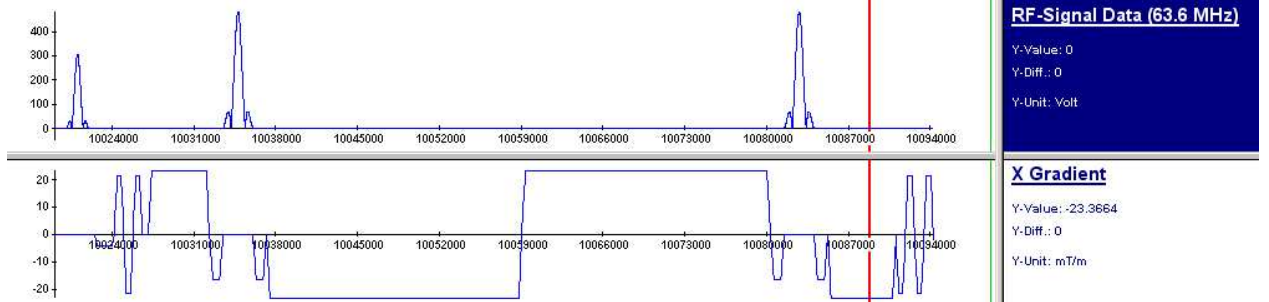


Figure 10: Twice refocused spin-echo (TRSE) diffusion weighted sequence applied to acquire the diffusion weighted MR images. The diagram presented here corresponds to one of diffusion directions,  $(1, 0, 0)$ . For clarity, only the diffusion gradient along the  $x$ -axis is displayed.

## References

- [1] Abragam A, “The Principles of Nuclear Magnetism”, Oxford University Press, London, 1961.
- [2] Ahn CB, Cho ZH, “Analysis of eddy currents induced artifacts and temporal compensation in nuclear magnetic resonance imaging”, *IEEE Trans Med Imaging*, 1991;10:47-52.
- [3] Alexander AL, Lee JE, Lazar M, Boudos R, DuBray MB, Oakes TR, Miller JN, Lu J, Jeong EK, McMahon WM, Bigler ED, Lainhart JE, “Diffusion tensor imaging of the corpus callosum in autism”, *NeuroImage*, 2007;34:61-73.
- [4] Anderson AW, “Measurement of fiber orientation distributions using high angular resolution diffusion imaging”, *Magn Reson Med*, 2005;54:1194-1206.
- [5] Basser PJ, Pajevic S, Pierpaoli C, Duda J, Aldroubu A, “In vivo fiber tractography using DT-MRI data”, *Magn Reson Med*, 2000;44:625-632.
- [6] Basser PJ, “Relationships between diffusion tensor and q-space MRI”, *Magn Reson Med*, 2002;47:392-397.
- [7] Batchelor PG, Hill DLG, Calamante F, Atkinson D, “Study of connectivity in the brain using the full diffusion tensor from MRI”, in *Proceedings of the 17th International Conference on Information Processing in Medical Imaging*, pp. 121-133, Springer-Verlag, New York, 2001.
- [8] Bowtell R, Mansfield P, “Gradient coil design using active magnetic screening”, *Magn Reson Med*, 1991;17:15-21.
- [9] Conturo TE, Lori NF, Cull TS, Akbudak E, Snyder AZ, Shimony JS, McKinstry RC, Burton H, Rachle ME, “Tracking neuronal fiber pathways in the living human brain”, *Proc Natl Acad Sci (USA)*, 1999;96:10422-10427.
- [10] Descoteaux M, Angelino E, Fitzgibbons S, Deriche R, “Apparent diffusion coefficients from high angular resolution diffusion imaging: estimation and applications”, *Magn Reson Med*, 2006;56:395-410.
- [11] D’Arceuil H, Crespigny A, “The effects of brain tissue decomposition on diffusion tensor imaging and tractography”, *NeuroImage*, 2007;36:64-68.
- [12] Einstein A, “The foundation of the general theory of relativity”, *Annalen der Physik*, 1916.
- [13] Frank LR, “Anisotropy in high angular resolution diffusion-weighted MRI”, *Magn Reson Med*, 2001;45:935-939.
- [14] Frank LR, “Characterization of anisotropy in high angular resolution diffusion-weighted MRI”, *Magn Reson Med*, 2002;47:1083-1099.

- [15] Gilmore JH, Lin W, Corouge I, Vetsa YSK, Smith JK, Kang C, Gu H, Hamer RM, Lieberman JA, Gerig G, "Early postnatal development of corpus callosum and corticospinal white matter assessed with quantitative tractography", *AJNR Am J Neuroradiol*, 2007;28:1789-1795.
- [16] Hahn EL, "Spin Echoes", *Phys. Rev*, 1950;80:580-594.
- [17] Hofer S, Frahm J, "Topography of the human corpus callosum revisited-comprehensive fiber tractography using diffusion tensor magnetic resonance imaging", *NeuroImage*, 2006;32:989-994.
- [18] Gray H, "Gray's Anatomy of the Human Body", Lea & Febiger, Philadelphia, 1918:828-829.
- [19] Hosey T, Williams G, Ansoorge R, "Inference of multiple fiber orientations in high angular resolution diffusion imaging", *Magn Reson Med*, 2005;54:1480-1489.
- [20] Jellison BJ, Field AS, Medow J, Lazar M, Salamat MS, Alexander AL, "Diffusion tensor imaging of cerebral white matter a pictorial review of physics, fiber tract anatomy, and tumor imaging patterns", *AJNR Am J Neuroradiol*, 2004;25:356-369.
- [21] Kang N, Zhang J, Carlson ES, "Parallel simulation of anisotropic diffusion with human brain DT-MRI Data", *Computers and Structures*, 2004;82:2389-2399.
- [22] Kang N, Zhang J, Carlson ES, Gembris D, "White matter fiber tractography via anisotropic diffusion simulation in the human brain", *IEEE Transactions on Medical Imaging*, 2005;24:1127-1137.
- [23] Laundre BJ, Jellison BJ, Badie B, Alexander AL, Field AS, "Diffusion tensor imaging of the corticospinal tract before and after mass resection as correlated with clinical motor findings: preliminary data", *AJNR Am J Neuroradiol* 2005;26:791-796.
- [24] Lee JS, Han MK, Kim SH, Kwon OK, Kim JH, "Fiber tracking by diffusion tensor imaging in corticospinal tract stroke: topographical correlation with clinical symptoms", *NeuroImage*, 2005;26:771-776.
- [25] Liu C, Bammer R, Acar B, Moseley ME, "Characterizing non-Gaussian diffusion by using generalized diffusion tensors", *Magn Reson Med*, 2004;51:924-937.
- [26] Mattiello J, Basser PJ, Le Bihan D, "Analytical expressions for the b matrix in NMR diffusion imaging and spectroscopy", *Journal of Magnetic Resonance*, 1994;108:131-141.
- [27] Mattiello J, Basser PJ, Le Bihan D, "The b matrix in diffusion tensor echo-planar imaging", *Magn Reson Med*, 1997;37:292-300.
- [28] Meijerink JA, van der Vorst HA, "An iterative solution method for linear systems of which the coefficient matrix is a symmetric M-matrix", *Math Comput*, 1977;31:148-162.
- [29] Mori S, van Zijl PCM, "Fiber tracking principles and strategies: A technical review", *NMR in Medicine*, 2002;15:468-480.

- [30] Nimsky C, Ganslandt O, Merhof D, Sorensen AG, Fahlbusch R, “Intraoperative visualization of the pyramidal tract by diffusion-tensor-imaging-based fiber tracking”, *NeuroImage*, 2006;30:1219-1229.
- [31] O’Donnell L, Haker S, Westin CF, “New approaches to estimation of white matter connectivity in diffusion tensor MRI: elliptic PDEs and geodesics in a tensor-warped space”, *MICCAI*, 2m02.
- [32] Özarslan E, Mareci TH, “Generalized diffusion tensor imaging and analytical relationships between diffusion tensor imaging and high angular resolution diffusion imaging”, *Magn Reson Med*, 2003;50:955-965.
- [33] Özarslan E, Vemuri BC, Mareci T, “Fiber orientation mapping using generalized diffusion tensor imaging”, *IEEE Intl. Symposium on Biomedical Imaging (ISBI)*, 2004;1:1036-1039.
- [34] Reese TG, Heid O, Weisskoff RM, Wedeen VJ, “Reduction of eddy-current-induced distortion in diffusion MRI using a twice-refocused spin echo”, *Magn Reson Med*, 2003;49:177-182.
- [35] Robertson, B, “Spin-echo decay of spins diffusion in a bounded region”, *Phys Rev*, 1966;151:273-277.
- [36] Rose SE, McMahon KL, Janke AL, ODowd B, de Zubicaray G, Strudwick MW, Chalk JB, “MRI diffusion indices and neuropsychological performance in mild cognitive impairment”, *Journal of Neurology, Neurosurgery and Psychiatry*, 2006;77:1122-1128.
- [37] Slichter CP, “Principles of Magnetic Resonance”, Springer-Verlag, 1978.
- [38] Stejskal EO, Tanner JE, “Spin diffusion measurements: spin echoes in the presence of a time-dependent field gradient”, *J. Chem. Phys.* 1965;42:288-292.
- [39] Tommasi G, Krack P, Fraix V, Le Bas JF, Chabardes S, Benabid AL, Pollak P, “Pyramidal tract side effects induced by deep brain stimulation of the subthalamic nucleus”, *J Neurol Neurosurg Psychiatry*, 2008;79:813-819.
- [40] Torrey HC, “Bloch equations with diffusion terms”, *Phys. Rev*, 1956;104:563-565.
- [41] Tuch DS, “Diffusion MRI of Complex Tissue Structure”, PhD Thesis, Harvard University-MIT, Cambridge, MA, 2002.
- [42] Tuch DS, Reese TG, Wiegell MR, Makris N, Belliveau JW, Wedeen VJ, “High angular resolution diffusion imaging reveals intravoxel white matter fiber heterogeneity”, *Magn Reson Med*, 2002;48:577-582.
- [43] van der Vorst H, “Bi-CGSTAB: a fast and smoothly converging variant of Bi-CG for the solution of nonsymmetric linear systems”, *SIAM J. Sci. Stat. Comput.*, 1992;13:631-644.
- [44] Wiegell MR, Larsson HB, Wedeen VJ, “Fiber crossing in human brain depicted with diffusion tensor MR imaging”, *Radiology*, 2000;217:897-903.